Phys. Status Solidi A **210**, No. 10, 2159–2165 (2013) / **DOI** 10.1002/pssa.201329146

physica status solidi a
www.pss-a.com
applications and materials science

Effect of quenching rate on the average grain size and martensitic transformation temperature in rapidly solidified polycrystalline $Ni_{50}Mn_{37}Sn_{13}$ alloy ribbons

A. Quintana-Nedelcos[*,1], J. L. Sánchez Llamazares[,1], D. Ríos-Jara[1], A. G. Lara-Rodríguez[2], and T. García-Fernández[3]**

[1] Instituto Potosino de Investigación Científica y Tecnológica A.C., Camino a la Presa San José 2055, Col. Lomas 4ª sección, San Luis Potosi, SLP 78216, México
[2] Instituto de Investigaciones en Materiales, Universidad Nacional Autónoma de México, México, DF 04510, México
[3] Universidad Autónoma de la Ciudad de México, México, DF 09790, México

Received 1 March 2013, revised 22 May 2013, accepted 6 June 2013
Published online 17 July 2013

Keywords ferromagnetic shape memory alloys, grain-size effect, martensite phase transformation, melt spinning, Ni–Mn–Sn ribbons

[*] Corresponding author: e-mail aris.quintana@ipicyt.edu.mx, Phone: +52 444 2000, Fax: +52 444 7269
[**] e-mail jose.sanchez@ipicyt.edu.mx, Phone: +52 444 2000, Fax: +52 444 7269

The present investigation was undertaken to investigate the effect of quenching rate on the microstructure of $Ni_{50}Mn_{50-x}Sn_x$ ribbon alloys and its influence on the martensitic starting phase-transition temperature M_S. The study was performed on melt-spun ribbons of a ferromagnetic shape memory alloy (FSMA) of composition $Ni_{50}Mn_{37}Sn_{13}$ produced by varying the speed of the rotating copper wheel between 15 and 50 m s^{-1}. The resulting samples have a chemical composition close to the nominal one and at room temperature crystallize in a cubic single-phase austenite with the highly ordered $L2_1$-type crystal structure without a significant variation in the cell parameter. The average grain size varies between 1.4 and 7.3 μm, while M_S increased from 212 to 258 K. Our results suggest that in these materials the average grain size of the parent austenite phase limits the size of the martensite variants, giving rise to its stabilization, while a multivariant transformation mode is maintained.

1 Introduction Ferromagnetic shape memory alloys (FSMAs) have been extensively investigated over the last 15 years [1]. These materials show a structural martensitic transition (MT) from a higher-temperature parent phase (austenite; AST) to a lower-temperature phase (martensite; MST). Along with this structural phase transition, a magnetization jump occurs. A wide range of interesting physical phenomena may be associated with the MT, such as direct [2] and inverse [3, 4] giant magnetocaloric effects; a large magnetoresistance change [5, 6]; and a magnetic-field-induced reverse martensitic transformation [4, 7, 8]. The latter makes these materials of considerable scientific and technological interest. The tuning of the starting martensitic transformation temperature M_S around a desired temperature, for instance room temperature, is an important aspect related to their potential technological applications.

The most studied FSMA are those of the Ni–Mn–Ga system [1, 9]. However, important efforts have been carried out to develop Ga-free FSMA alloys [10–12]. Such work has been mainly focused on Heusler Ni–Mn–X alloys, with X = Sn, In, or Sb [10–13]. These materials were first reported by Sutou et al. in 2004 [10]. Most of the work reported in the literature to tune M_S in these materials involves: (i) changes of the Mn/X ratio [11–13]; (ii) the partial atomic substitution of one (or more) of the three main elements of the alloy by other elements [14–18]; and (iii) the introduction of elements of small atomic radius into interstitial sites [19, 20]. In addition, it is also known that different models correlate the average grain size of a polycrystalline shape memory alloy with M_S [21–24], but, as far as we know, an understanding of the M_S dependence with the average grain size of Ni–Mn–X alloys (X = Sn, In, Sb)

has been less considered. The two factors to which M_S has been mainly related are: the density of volume and surface crystal defects [21, 22] and the probability of nucleation of the MST phase in the austenitic matrix [23]. Another explanation may be that the chemical free energy must overcome the strain energy to initiate the crystalline transformation [24]. In such a case, the occurrence of the transformation in a monovariant or multivariant mode is critical, where a multivariant mode favors the cancellation of the strain energy through the self-accommodation of the variants [24].

Rapid solidification by using the melt-spinning technique is an effective one-step process to obtain single-phase alloy ribbons in the $Ni_{50}Mn_{50-x}Sn_x$ system [25, 26]. When these materials are produced by means of this technique [25], the microstructure is considerably refined in size and they show lower M_S in comparison with bulk alloys with a similar composition [11, 27]. This should be mainly associated with the difference in the average grain size $<d>$ between ribbons and bulk alloys. For sputtered $Ni_{50}Mn_{35}Sn_{15}$ thin films with nanometric particles, M_S increases as the average grain size increases [28]. However, a study as well as an attempt to understand the effect of quenching rate on the average grain size of Heusler $Ni_{50}Mn_{50-x}Sn_x$ alloys and its influence on the martensitic starting phase-transition temperature M_S in rapidly solidified polycrystalline has not been reported yet. This has been the aim of the present work and with such a purpose, the alloy $Ni_{50}Mn_{37}Sn_{13}$ was produced by the melt-spinning method; different cooling rates were obtained by quenching the alloy on a copper wheel with different tangential wheel speeds.

2 Experimental Bulk samples of 3 g of the alloy with nominal composition $Ni_{50}Mn_{37}Sn_{13}$ were prepared by Ar arc melting from highly pure starting material (>99.98%). Samples were melted three times to ensure a good homogeneity. As-spun ribbons were obtained by melt spinning under a controlled highly pure argon environment. The copper wheel linear speed v was varied from 15 to 50 m s^{-1}. To ensure a well-ordered crystalline structure for austenite, the samples were encapsulated in quartz tubes under an argon atmosphere and annealed for 10 min at 1123 K. Hereafter, the annealed ribbons obtained at $v = 15$, 30, 40, and 50 m s^{-1} are referred to as Sn15TT, Sn30TT, Sn40TT, and Sn50TT, respectively. Their average thickness $<t>$, measured from SEM micrographs, was 28, 17, 14, and 7 μm, respectively.

Microstructural characterization and the determination of the chemical composition by energy-dispersive X-ray spectroscopy (EDS) were done in a Phillips model XL-30 scanning electron microscope (SEM). To determine the elemental chemical composition, the EDS detector was calibrated with a bulk Ni–Mn–Sn sample of a known composition that was similar to the samples studied ($Ni_{50}Mn_{37}Sn_{13}$). SEM images of the typical microstructure of ribbons were taken from the contact (CS) and noncontact surface (NCS) of the ribbons with the copper wheel and from their cross section. More than 300 measurements were made to estimate the average diameter in order to calculate the average grain size $<d>$, and the average grain volume $<V>$. Structural analysis by X-ray diffraction (XRD) was performed at room temperature using a Bruker diffractometer model D8 ADVANCE (using CuKα radiation) in order to check the sample monophasicity and crystal structure of AST. Phase-transition studies were carried out by differential scanning calorimeter (DSC) using a TA Instruments model Q200. DSC curves for 10 mg samples were measured with a heating/cooling rate of 10 K min^{-1}.

Magnetization measurements were performed from 10 to 400 K using a Quantum Design PPMS-9T platform with the vibrating sample magnetometer module. Field-cooling (FC), and field-heating (FH) thermomagnetic curves were measured for applied static magnetic fields of $\mu_0 H = 5$ mT and $\mu_0 H = 5$ T with a heating or cooling rate of 1 K min^{-1}.

3 Results and discussion Figure 1a shows the room-temperature XRD patterns obtained for the samples studied

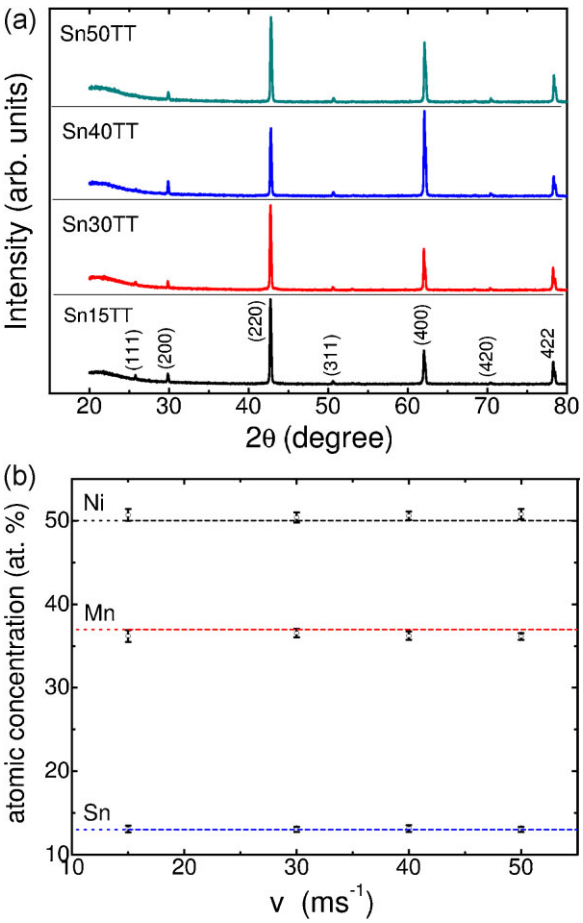

Figure 1 XRD patterns (a) and Ni, Mn, and Sn atomic concentration of the ribbons as a function of the linear speed of the cooper wheel v (b) for Sn15TT, Sn30TT, Sn40TT, and Sn50TT ribbons. The solid lines represent the nominal elemental atomic concentration (*i.e.*, 50 at.% Ni, 37 at.% Mn, and 13 at.% Sn).

in this work. All the alloys are single-phase (*i.e.*, there were no secondary phases detected). The patterns can be satisfactorily indexed on the basis of a cubic single-phase austenite phase with the highly ordered $L2_1$-type crystal structure. The lattice parameter a for samples Sn15TT, Sn30TT, Sn40TT, and Sn50TT, are 5.97(2), 5.97(3), 5.96 (9), and 5.96(7) Å, respectively. These a values are in good agreement with those previously reported for melt-spun ribbons of close chemical composition [25–29].

It is well known that for Ni–Mn-based alloys the MT transition temperature is strongly affected by the Mn–Mn interatomic distances [19, 30, 31]. In our work, the difference observed in the lattice parameter a between samples is small (*i.e.*, around 0.005 Å), suggesting that the M_S variation is not related to the modification of Mn–Mn interatomic distances. Furthermore, another factor that can affect M_S is the average valence electron concentration per atom e/a [11, 32], an estimation is usually made on the basis of the average chemical composition determined by EDS. The average atomic concentration for each element, together with the corresponding error bar, is shown in Fig. 1b. These results were based on more than 30 measurements from each sample on both ribbon surfaces and also their cross-section. The standard deviation obtained for the elemental chemical composition (as determined by EDS) was 0.5–0.6 at.% for Ni, 0.4–0.5 at.% for Mn, and 0.3–0.4 at.% for Sn. Hence, the EDS study shows that the four samples studied exhibit a high degree of homogeneity in their average elemental composition, which is very close to the nominal one. The small difference in the elemental chemical composition between nominal and measured values is mainly attributed to Mn evaporation during the radio-frequency induction-melting process used to fabricate the melt-spun ribbons. Considering the number of valence electrons for Ni, Mn, and Sn (*i.e.*, 10, 7, and, 4, respectively), the calculated e/a for our ribbon samples Sn15TT, Sn30TT, Sn40TT, and Sn50TT, are 8.13, 8.12, 8.12, and 8.13, respectively. This indicates that this parameter does not exhibit a significant variation, suggesting that the M_S variation is not associated with a change in this parameter. However, at this point we must also consider that EDS is a semiquantitative technique that allows the determination of the elemental chemical composition with an accuracy of 0.1% (*i.e.*, atomic percentage or weight percent) and how this uncertainty can vary e/a and the resulting M_S value. Assuming a difference in the Mn (or Ni) content of ±0.1 at.%, and taking into account the nearly linear e/a dependence of the M_S temperature given in Ref. [11], we obtained that M_S only varies by ±2 K.

Figure 2 shows the FC and FH magnetization as a function of temperature $M(T)$ curves under low and high applied magnetic field of 5 mT (a), and 5 T (b), respectively. In both sets of curves the two well-distinct ferromagnetic regions characteristic of MST and AST, as well as the jump in magnetization associated to the structural phase transition, are observed. From the FH $M(T)$ curves at 5 mT for samples SnTT15 and SnTT30 the magnetic transition of MST, from a dominant ferromagnetic to a weak magnetic state, has been

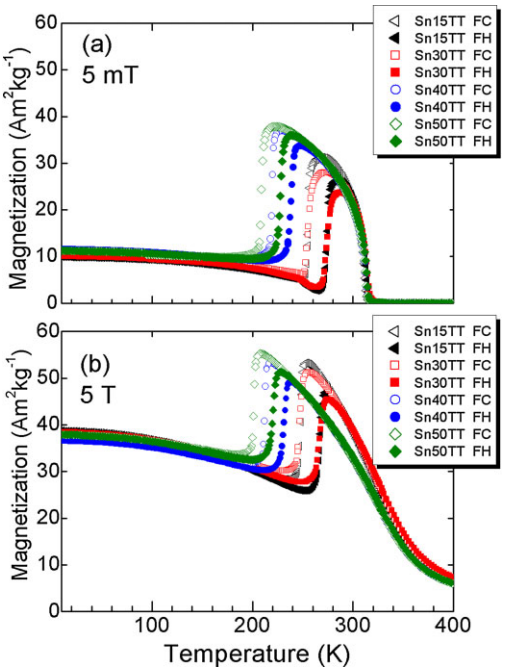

Figure 2 FC and FH temperature dependence of the magnetization $M(T)$ of Sn15TT, Sn30TT, Sn40TT, and Sn50TT ribbons at 5 mT (a) and 5 T (b).

estimated to be 260 K. For all the samples the Curie temperature of AST T_C^A is 313 K. It is worth mentioning that the main difference between the curves lies in the shift of the characteristic starting and finish structural transition temperatures of the direct (reverse) MT, namely M_S and M_f (A_S and A_f) towards a lower temperature with increasing quenching rate. In addition, notice that below M_f the FH and FC pathways of the curves $M(T)$ measured at 5 T tend to overlap in the martensitic existence region, indicating that all the samples show a similar saturation magnetization. The latter is a further indication regarding the similar chemical composition of the samples.

SEM micrographs of the free surface of ribbons and fracture morphology (insets) are shown in Fig. 3. The calculated average grain size $<d>$ in the CS and NCS for heat-treated ribbons is listed in Table 1. As reported previously [25, 33], there is no significant grain-size dependence with the cooling rate on the CS. For CS, the cooling rate is so high that the kinetic grain growth is limited by the rate of crystallization, forming a very thin layer of small grains, which is not representative of the bulk of the ribbon. However, for NCS an increase of $<d>$ with a lower cooling rate is clearly observed. As expected, with the decrease in the cooling rate, grain growth kinetics is favored.

Figure 4 shows the DSC cooling curves for the Sn15TT, Sn30TT, Sn40TT, and Sn50TT samples (*i.e.*, the peaks in the curves correspond to the forward MT). The characteristic structural transition temperatures of the direct and reverse martensitic transformation, usually referred to as martensitic starting M_S, martensitic finish M_f, austenitic starting A_S, and

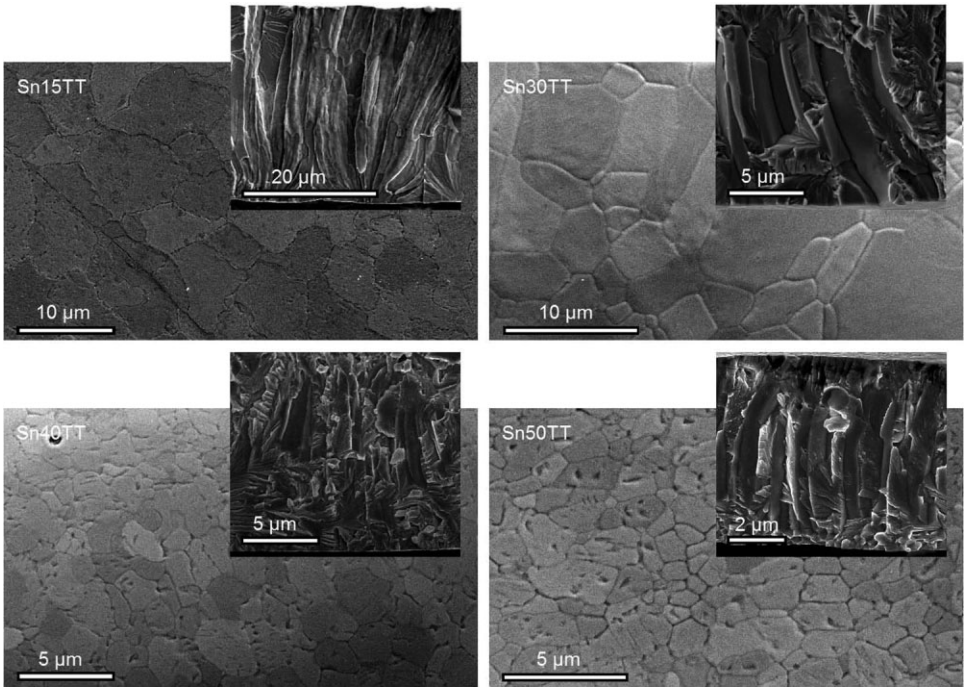

Figure 3 Typical SEM images showing the surface microstructure of ribbons on their free surface (*i.e.*, NCS). Insets: fractured cross-section. The samples were annealed for 10 min at 1123 K.

Table 1 The average grain size $<d>$ with its standard deviation for the CS and NCS and the corresponding values of M_S, M_f, A_S, and A_f obtained for the heating and cooling DSC curves for annealed samples Sn15TT, Sn30TT, Sn40TT, and Sn50TT.

sample	$<d>$ (μm)		std. dev.		M_S (K)	M_f (K)	A_S (K)	A_f (K)
	CS	NCS	CS	NCS				
Sn15TT	0.9	7.3	0.3	3.7	258	249	267	278
Sn30TT	1.1	3.2	0.4	1.5	258	245	266	280
Sn40TT	0.9	1.8	0.3	0.7	220	212	230	243
Sn50TT	0.9	1.4	0.4	0.6	212	204	225	233

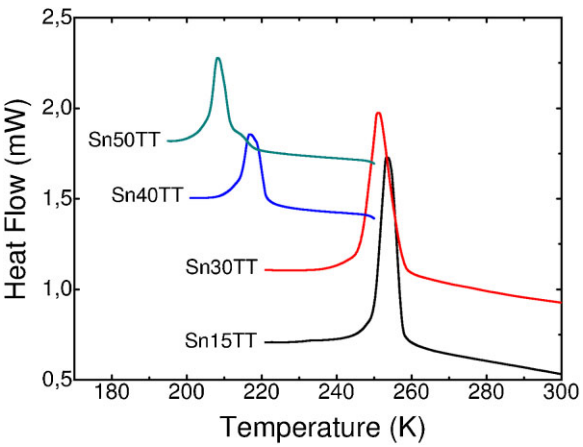

Figure 4 DSC cooling curves for the ribbon samples studied (*i.e.*, the peaks represent the forward martensitic transformation).

austenitic finish A_f temperatures are listed in Table 1 (*i.e.*, M_S, M_f, A_S, and A_f). As shown, M_S shifts to lower temperatures for the ribbons solidified at higher cooling rates (*i.e.*, M_S increases with the increment of $<d>$). At the same time, the area of the peaks (*i.e.*, the heat exchange, quantification of Q is tabulated in Table 2) becomes smaller for ribbons solidified at higher cooling rates. The latter indicates that smaller amounts of heat are needed to complete the structural transformation.

From a thermodynamic point of view, the martensitic transformation occurs when additional chemical energy exceeds the difference in the Gibbs free energy ΔG between the austenitic and martensitic states. Hence, when ΔG increases a reduction in M_S should be expected [24]. In fact, the different martensitic variants form to minimize the elastic energy E_{el} associated with the deformation of the system. In a conventional multivariant mode, E_{el} is partially cancelled due to the self-accommodation of the variants. With the decrease of the austenite grain size, a smaller number of

Table 2 Values of M_S and Q obtained from the DSC curves, as well as the calculated thermodynamical parameters of T_0, ΔH, ΔS, $E_{el}/\Delta H$, and $W_d/\Delta H$ for the studied samples.

sample	Sn15TT	Sn30TT	Sn40TT	Sn50TT
M_S (K)	258	258	220	212
T_0 (K)	268	269	232	223
Q (J g^{-1})	4.264	3.066	0.867	0.353
ΔH (J g^{-1})	4.504	3.279	0.927	0.376
ΔS (J g^{-1} K^{-1})	0.017	0.012	0.004	0.002
$E_{el}/\Delta H$ (%)	1.9	2.5	2.3	1.8
$W_d/\Delta H$ (%)	7.1	8.0	8.9	9.4

martensitic variants form into the grain, and consequently, the partial cancellation of the E_{el} due to the self-accommodation of the martensitic variants formed is smaller, thereby requiring a greater energy expenditure to initiate the martensitic transformation [34].

The heat exchange Q during the transformation process is not exactly equal to the change in enthalpy ΔH of the transformation. The difference between Q and ΔH is determined by the contribution of E_{el} and the irreversibly dissipated energy W_d,

$$Q = \int_{M_S/A_S}^{M_f/A_f} T(\mathrm{d}S) = \Delta H - E_{el} + W_d. \quad (1)$$

The retained energy E_{el} and the irreversibly dissipated energy W_d involved in the MT can be quantified by the relative fraction that they represent of the total enthalpy of the transformation, $E_{el}/\Delta H$ and $W_d/\Delta H$, respectively. For practical purposes, a good estimation of both terms can be made in accordance with reference [35]:

$$E_{el} = 1/4\Delta S[(A_f - A_S) + (M_S - M_f)], \quad (2)$$

$$W_d = 1/2\Delta S\,[(A_f + A_S) - (M_S + M_f)]. \quad (3)$$

Table 2 summarizes the characteristic values of the thermodynamical parameters associated with the MT, namely M_S, T_0, Q, ΔH, ΔS, $E_{el}/\Delta H$, and $W_d/\Delta H$. Here, T_0 is the thermodynamic equilibrium temperature defined as $T_0 = (M_S + A_f)/2$.

As is shown in Table 2, the fraction of ΔH that remains in the system as elastic energy is small ($\sim$2%), and does not show a monotonous relationship with T_0. Moreover, from the thermodynamic equilibrium condition ($\Delta G = 0 = \Delta H - T_0\Delta S$), it follows that $T_0 = \Delta H/\Delta S$, in such a way that T_0 decreases either, if ΔH decreases and/or ΔS increases. Indeed, we find that T_0 tends to decrease with a decrease of the average grain size, but the decrease observed in ΔS is inconsistent with this hypothesis. Hence, the monovariant thermodynamic hypothesis seems not to be a plausible explanation for the observed reduction of M_S with $<d>$ in our samples. So, a multivariant mechanism must be considered for a correct explanation of the $<d>$ dependence of M_S in our samples. In fact, the typical plate-like stripes of the multivariant martensitic mode have been observed in previous TEM studies by Zheng et al. [33] and Chen et al. [36] in $Ni_{49}Mn_{39}Sn_{12}$ and $Ni_{38}Co_{12}Mn_{41}Sn_9$ melt-spun alloy ribbons, respectively, and by Esakki Muthu et al. [37] in $Ni_{50}Mn_{37}Sn_{13}$ bulk alloys.

Guimarães and Rios considered a phenomenological model that correlates M_S with the average grain size, in which the nucleation of martensitic domains occurs in the vicinity of the defects of the austenitic grains [22]. The grain boundaries are considered as surface defects that provide favorable conditions for nucleating the martensitic phase within the austenitic matrix. The main conclusion is that small grains have a stabilizing effect of the austenitic phase because they limit the volume of the individual martensite variants [22]. In connection with this, a relationship of the type $\rho \sim 1/D$ has been reported in Ref. [21], where ρ is the density of dislocations and D is the diameter of the austenitic grain. A smaller average grain size increases the crystal defect density, giving rise to a greater impediment to the occurrence of martensitic transformation due to the increase of the potential barrier for the structural phase transition. In Ref. [23], it is shown that $p = 1 - \exp(-\lambda v)$, where p is the transformed fraction of an individual crystal into martensite phase, v the volume of the grain, and λ is the probability of martensite nucleation per unit volume (λ is a function of temperature). This expression states that the probability of nucleation decreases exponentially with a decrease in the grain size. Finally, in Ref. [38] the following empirical equation was proposed:

$$M_S^0 - M_S = \frac{1}{b}\ln\left[\frac{1}{a * V_a}\left\{\exp\left(-\frac{\ln(1-f)}{m}\right) - 1\right\} + 1\right], \quad (4)$$

where a and b are fitting constants and equal to 5.58 and 6.68, respectively, V_a is the grain volume of the austenitic phase, m is the plate aspect ratio of the grain (length/diameter; $m = 4$), f the minimum fraction of austenite transformed into the martensite phase required to detect the beginning of the MT (usually taken as $f \cong 0.01$), M_S^o is the martensitic starting temperature for an infinitely large austenitic grain, and M_S is the martensitic starting phase-transition temperature.

Figure 5 shows the relationship between M_S and $<V>$ for the samples produced (represented by the black squares), and the numerical fitting obtained from Eq. (4) (red solid line). The values reported by Santos et al. [25] (blue circle), is also presented to illustrate that they are within the trend. It can be seen that despite the rough approximation both M_S and the estimated average volume $<V>$ follow the trend established by this model. This suggests that with a decrease in the average grain size, an increase of the crystal defects density takes place, which stabilizes the austenitic phase.

4 Conclusions Melt-spun ribbons of the alloy $Ni_{50}Mn_{37}Sn_{13}$ with a different average grain size were produced by rapid solidification using the melt-spinning

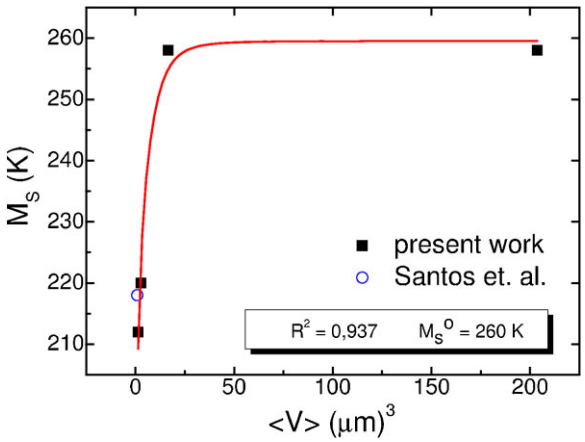

Figure 5 Dependence of M_S with the average grain volume $<V>$ for the samples studied in the present work (black squares). The value reported by Santos et al. [25] (blue circle) is also represented. The solid red line was calculated using Eq. (4) for fitting purposes.

technique. The ribbons have nearly constant elemental chemical composition and cubic cell parameters for austenite at room temperature. The average grain size varies between 1.4 and 7.3 μm. The reduction in the average grain size is accompanied by a decrease in M_S from 258 to 212 K (*i.e.*, 46 K) demonstrating that the structural transition temperatures can be tuned within certain limits by controlling this microstructural parameter; additionally, the average grain volume $<V>$ has been correlated with M_S. The dependence found suggests that in these materials the decreasing of austenite grain size, which is accompanied by an increase in the density of crystal defects, limits the size of the martensite variants, contributing to the austenite stabilization, while a multivariant transformation mode is maintained.

Acknowledgements The authors acknowledge financial support received from CONACYT, Mexico, under projects CB-2010-01-157541 and CB-2012-176705, ICyTDF, UACM, and Gobierno del Distrito Federal-Mexico, and Laboratorio Nacional de Investigaciones en Nanociencias y Nanotecnología (LINAN, IPICYT). Technical support received from G. J. Labrada-Delgado and Rivera-Escoto is recognized.

References

[1] J. Pons, E. Cesari, C. Seguí, F. Masdeu, and R. Santamarta, Mater. Sci. Eng. A **481–482**, 57–65 (2008).
[2] X. Zhou, W. Li, H. P. Kunkel, and G. Williams, J. Phys.: Condens. Matter **16**, L39–L44 (2004).
[3] T. Krenke, E. Duman, M. Acet, E. F. Wassermann, X. Moya, L. Mañosa, and A. Planes, Nature Mater. **4**, 450–454 (2005).
[4] T. Krenke, E. Duman, M. Acet, E. Wassermann, X. Moya, L. Mañosa, A. Planes, E. Suard, and B. Ouladdiaf, Phys. Rev. B **75**, 104414 (2007).
[5] V. K. Sharma, M. K. Chattopadhyay, K. H. B. Shaeb, A. Chouhan, and S. B. Roy, Appl. Phys. Lett. **89**, 222509 (2006).
[6] K. Koyama, H. Okada, and K. Watanabe, Appl. Phys. Lett. **89**, 182510 (2006).
[7] K. Inoue, K. Enami, Y. Yamaguchi, and K. Ohoyama, J. Phys. Soc. Jpn. **69**, 3485–3488 (2000).
[8] K. Koyama, K. Watanabe, T. Kanomata, R. Kainuma, K. Oikawa, and K. Ishida, Appl. Phys. Lett. **88**, 132505 (2006).
[9] O. Söderberg, I. Aaltio, Y. Ge, O. Heczko, and S. P. Hannula, Mater. Sci. Eng. A **481–482**, 80–85 (2008).
[10] Y. Sutou, Y. Imano, N. Koeda, T. Omori, R. Kainuma, K. Ishida, and K. Oikawa, Appl. Phys. Lett. **85**, 4358 (2004).
[11] T. Krenke, M. Acet, E. Wassermann, X. Moya, L. Mañosa, and A. Planes, Phys. Rev. B **72**, 014412 (1–9), (2005).
[12] T. Krenke, M. Acet, E. Wassermann, X. Moya, L. Mañosa, and A. Planes, Phys. Rev. B **73**, 174413 (2006).
[13] J. Du, Q. Zheng, W. J. Ren, W. J. Feng, X. G. Liu, and Z. D. Zhang, J. Phys. D: Appl. Phys. **40**, 5523–5526 (2007).
[14] D. H. Wang, C. L. Zhang, H. C. Xuan, Z. D. Han, J. R. Zhang, S. L. Tang, B. X. Gu, and Y. W. Du, J. Appl. Phys. **102**, 013909 (2007).
[15] A. K. Nayak, K. G. Suresh, and A. K. Nigam, J. Appl. Phys. **107**, 09A927 (2010).
[16] D. H. Wang, C. L. Zhang, Z. D. Han, H. C. Xuan, B. X. Gu, and Y. W. Du, J. Appl. Phys. **103**, 033901 (2008).
[17] Z. Liu, Z. Wu, H. Yang, Y. Liu, W. Wang, X. Ma, and G. Wu, Intermetallics **19**, 1605–1611 (2011).
[18] I. Dubenko, T. Samanta, A. Kumar Pathak, A. Kazakov, V. Prudnikov, S. Stadler, A. Granovsky, A. Zhukov, and N. Ali, J. Magn. Magn. Mater. **324**, 3530–3534 (2012).
[19] H. C. Xuan, D. H. Wang, C. L. Zhang, Z. D. Han, B. X. Gu, and Y. W. Du, Appl. Phys. Lett. **92**, 102503 (2008).
[20] F. X. Hu, J. Wang, L. Chen, J. L. Zhao, J. R. Sun, and B. G. Shen, Appl. Phys. Lett. **95**, 112503 (2009).
[21] J. P. Hirth, Met. Trans. **3**, 3047–3067 (1972).
[22] J. R. C. Guimarães and P. R. Rios, J. Mater. Sci. **45**, 1074–1077 (2009).
[23] G. B. Olson, K. Tsuzaki, and M. Cohen, Mater. Res. Soc. Symp. Proc. 129–148 (1987).
[24] K. Seki, H. Kura, T. Sato, and T. Taniyama, J. Appl. Phys. **103**, 063910 (2008).
[25] J. D. Santos, T. Sanchez, P. Alvarez, M. L. Sanchez, J. L. Sa´nchez Llamazares, B. Hernando, L. Escoda, J. J. Sunol, and R. Varga, J. Appl. Phys. **103**, 07B326 (2008).
[26] H. C. Xuan, K. X. Xie, D. H. Wang, Z. D. Han, C. L. Zhang, B. X. Gu, and Y. W. Du, Appl. Phys. Lett. **92**, 242506 (2008).
[27] D. L. Schlagel, W. M. Yuhasz, K. W. Dennis, R. W. McCallum, and T. A. Lograsso, Scr. Mater. **59**, 1083–1086 (2008).
[28] R. Vishnoi and D. Kaur, Surf. Coat. Technol. **204**, 3773–3782 (2010).
[29] I. Babita, R. Gopalan, S. Ram, and H. J. Fecht, Nanosci. Nanotechnol. Lett. **1**, 151–155 (2009).
[30] E. Şa ıoğlu, L. Sandratskii, and P. Bruno, Phys. Rev. B **70**, 024427 (2004).
[31] B. Himmetoglu, V. M. Katukuri, and M. Cococcioni, J. Phys.: Condens. Matter **24**, 185501 (2012).

[32] A. T. Zayak, W. A. Adeagbo, P. Entel, and K. M. Rabe, Appl. Phys. Lett. **88**, 111903 (2006).
[33] H. Zheng, D. Wu, S. Xue, J. Frenzel, G. Eggeler, and Q. Zhai, Acta Mater. **59**, 5692–5699 (2011).
[34] J. Ortín and A. Planes, J. Phys. IV **1**, C4–13 (1991).
[35] P. Shamberger and F. Ohuchi, Phys. Rev. B **79**, 1–9 (2009).
[36] F. Chen, Y. X. Tong, Y. J. Huang, B. Tian, L. Li, and Y. F. Zheng, Intermetallics **36**, 81–85 (2013).
[37] S. Esakki Muthu, N. V. Rama Rao, D. V. Sridhara Rao, M. Manivel Raja, U. Devarajan, and S. Arumugam, J. Appl. Phys. **110**, 023904 (2011).
[38] H. S. Yang and H. K. D. H. Bhadeshia, Scr. Mater. **60**, 493–495 (2009).